Low-Power-Consumption Short-Length and High-Modulation-Depth Silicon Electrooptic Modulator

Carlos Angulo Barrios, Vilson Rosa de Almeida, and Michal Lipson

***Abstract*—In this paper, we propose and analyze a novel compact electrooptic modulator on a silicon-on-insulator (SOI) rib waveguide. The device confines both optical field and charge carriers in a micron-size region. The optical field is confined by using a planar Fabry–Pérot microcavity with deep Si/SiO_2 Bragg reflectors. Carriers are laterally confined in the cavity region by employing deep-etched trenches. The refractive index of the cavity is varied by using the free-carrier dispersion effect produced by a p-i-n diode. The device has been designed and analyzed using electrical and optical simulations. Our calculations predict, for a 20-μm-long device, a modulation depth of around 80% and a transmittance of 86% at an operating wavelength of 1.55 μm by using an electrical power under dc conditions on the order of 25 μW.**

***Index Terms*—Bragg reflector, device modeling, Fabry–Pérot cavity, integrated optics, optical modulator, plasma dispersion effect, silicon optoelectronics.**

I. Introduction

SILICON-BASED photonic components working at 1.3- and 1.55-μm fiber-optic communications wavelengths for fiber-to-home interconnects and local area networks (LANs) are a subject of intensive research because of the possibility of integrating optical elements and advanced electronics together on a silicon substrate using bipolar or complementary metal–oxide–semiconductor (CMOS) technology [1]. The resulting optoelectronic integrated circuit (OEIC) should exhibit a better performance than optical and electrical circuits do when considered separately and present a significantly lower cost than those based on III–V semiconductor materials.

Si passive structures, such as waveguides, couplers, and filters have been extensively studied [2]–[4]. Less work has been reported on Si active (or tunable) integrated devices, such as modulators and switches, despite their importance as a means of manipulating light beams for information processing (e.g., coding–decoding, routing, multiplexing, timing, logic operations, etc.) in integrated optic circuits. Some Si-based thermooptic [5], [6] and electrooptic [7]–[20] active devices have been demonstrated. In thermooptic devices, the refractive index of Si is modulated by varying the temperature, inducing a phase modulation which, in turn, is used to produce an intensity modulation at the output of the device. For Si, the thermal change of the real optical refractive index is large [5]. Nevertheless, the thermooptic effect is rather slow and can only be used at up to 1-MHz modulation frequencies [6]. For higher modulation frequencies, up to a few hundred megahertz, electrooptic devices are required.

Most of the proposed electrooptic devices exploit the free carrier dispersion effect [21] to change both the real refractive index and optical absorption coefficient. This is because the unstrained pure crystalline Si does not exhibit linear electrooptic (Pockels) effect, and the refractive-index changes due to the Franz–Keldysh effect and Kerr effect are very weak. In free-carrier absorption modulators (FCAM), changes in the optical absorption of the structure are directly transformed into an output intensity modulation [18]. Phase modulation in a specific region of optical devices, such as Mach–Zehnder modulators, total-internal-reflection (TIR)-based structures, cross switches, Y switches and Fabry–Pérot (F-P) resonators, is also used to modulate the output intensity [7]–[20].

Free-carrier concentration in electrooptic devices can be varied by injection, accumulation, depletion, or inversion of carriers. Si-based electrooptic modulators (EOMs) based on p-i-n diodes, metal–oxide–semiconductor field-effect transistors (MOSFETs) and bipolar-mode field-effect transistor (BMFET) structures have been proposed [7]–[20], [22], [23]. Table I shows a comparison of all-silicon electrooptic intensity modulators and switches reported in the literature. Most of the listed devices present some common features: they require long interaction distances and injection current densities higher than 1 kA/cm^2 in order to obtain a significant modulation depth. Long interaction lengths are undesirable in order to achieve high levels of integration and miniaturization for fabricating low-cost compact chips. High current densities may induce thermooptic effect due to heating of the structure and cause an opposite effect on the refractive-index change as that produced by free-carrier dispersion, reducing its effectiveness. There is therefore an urgent need, from the integration point of view, for structures that can be implemented in a micron-size region offering low current density, low power consumption, and high modulation depth.

Microcavities allow for the confinement and enhancement of the optical field in a very small region. The transmission of these structures near their resonance is highly sensitive to small index changes in the cavity, making microcavities adequate for intensity modulation applications in a short length [15]. In addition, since the refractive-index modulation can be confined to the cavity region, the electrical power to produce the desired phase change can be made very small.

Manuscript received September 6, 2002; revised December 18, 2002. This work was supported in part by the Alliance for Nanomedical Technologies, Air Force Office of Scientific Research, and in part by the Defense Advanced Research Project Agency under Contract No. F49620-02-1-0396.

The authors are with the School of Electrical and Computer Engineering, Cornell University, Ithaca, NY 14853 USA.

Digital Object Identifier 10.1109/JLT.2003.810090

0733-8724/03$17.00 © 2003 IEEE

TABLE I
SILICON ELECTROOPTIC ACTIVE DEVICES REPORTED IN THE LITERATURE (FCAM=FREE-CARRIER ABSORPTION MODULATOR; F-P=FABRY–PÉROT; TIR=TOTAL INTERNAL REFLECTION; ZGDC=ZERO GAP DIRECTIONAL COUPLER; M=AMPLITUDE MODULATION DEPTH; J=CURRENT DENSITY; t_s=SWITCHING TIME; V.D.= VERTICAL DEVICE; DEM/(D)=DEMONSTRATED; PROP/(P)=PROPOSED)

Year	Author	Electrical structure	Optical structure	M (%)	J (kA/cm^2)	Power (mW)	t_s (ns)	Length (μm)	Dem./ Prop.
1987	Lorenzo et al. [7]	p-i-n	Cross switch	50	1.26	-	-	2000	D
1989	Hemenway et al. [8]	p-i-n	Mach-Zehnder	30	100.0	-	18	v.d.	D
1991	Treyz et al. [9]	p-i-n	FCAM	75	3.0	-	50	500	D
1991	Treyz et al [10]	p-i-n	Mach-Zehnder	65	1.6	-	<50	500	D
1991	Xiao et al. [11]	p-i-n	F-P	10	6.0	-	25	v.d.	D
1994	Liu et al. [12]	p-i-n	Y-switch	>90	9.0	-	200	800	D
1994	Liu et al. [13]	p-i-n	TIR-switch	>90	12.5	-	100	200	D
1995	Zhao et al. [14]	p-i-n	Mach-Zehnder	98	-	-	200	816	D
1995	Liu et al. [15]	p-i-n	F-P	80	-	-	-	20.9	P
1996	Zhao et al .[16]	p-i-n	ZGDC	97.2	1.027	123.7	210	1103	D
1997	Cutolo et al. [17]	p-i-n	Bragg reflector	50	-	4	24.7	3200	P
1997	Cutolo et al. [18]	BMFET	FCAM	20	2.3	126	6	1000	P
1997	Zhao et al. [19]	p-i-n	TIR	>88	8.8	-	110	190	D
2001	Coppola et al. [20]	p-i-n	Bragg reflector	94	-	0.3	5	3200	P

Carrier confinement in the active region of the electrooptic device is important in order to optimize the device performance. For example, the use of lateral trench isolation in a silicon p-i-n phase modulator has been predicted to improve both the dc and transient device performances [24]. This is because the lateral carrier diffusion that does not contribute to altering the refractive index in the central active region of the modulator is reduced, allowing a better use of the injected carriers. In addition, carrier confinement permits high-scale integration due to electrical isolation between neighbor devices.

We propose the use of the aforementioned advantages of microcavities (optical field confinement) and trench isolation (carrier confinement) in a planar silicon F-P cavity formed by high-index-contrast Si/SiO_2 distributed Bragg reflectors (DBRs) to design a compact low-drive-power and high-modulation-depth EOM in a silicon-on-insulator (SOI) ridge waveguide. The SOI ridge waveguide allows implementing a lateral p-i-n diode in the microcavity, and may exhibit optical losses less than 1.0 dB/cm at 1.55-μm wavelength [25].

This paper has been divided into the following sections. Section II describes the device structure. In Section III, the electrical and optical models used for the calculations are presented. In Section IV, results from the simulations are shown and discussed. This section is divided into electrical and optical characteristics. The electrical analysis includes dc and transient performance of the p-i-n/cavity configuration. The optical analysis comprises both the optical mode characteristics and the transmission properties of the device. Finally, a summary and conclusions are given in Section V.

II. DEVICE STRUCTURE

Fig. 1(a) and (b) shows a perspective and longitudinal-section schematics, respectively, of the EOM. For illustration purposes, the trenches down to the buried oxide (BOX) layer are drawn as empty in Fig. 1(a). In our simulations, these are assumed to be completely filled with SiO_2. The device consists of an F-P cavity formed by two DBRs in an SOI rib waveguide. The top silicon layer (device layer) is 1.5-μm-high (h_d) with an n-type background doping concentration of 10^{15} cm^{-3}. Both DBRs consist of the same number of Si/SiO_2 periods down to the BOX layer. The length of the Si and SiO_2 regions is denoted as L_{Si} and L_{ox}, respectively. Fig. 2 shows a schematic diagram of the cavity region. As in Fig. 1(a), the trenches are drawn as unfilled for better visualization. The rib width and height are chosen to be $w_{rib} = 1.5$ μm and $h_{rib} = 0.45$ μm, respectively. Two lateral trenches down to the BOX layer are assumed to be on both sides of the rib with a width of $w_{tr} = 150$ nm. The width of the cavity region delimited by the lateral trenches is W_{pin}. Heavily doped p^+ and n^+ regions are defined in the cavity region, at both sides of the rib, separated $w_{sep} = 0.5$ μm from the corresponding rib edge and extended to the corresponding lateral trench. A Gaussian doping profile is assumed for both highly doped regions with a maximum peak concentration of 10^{20} cm^{-3} at $y = [(h_d - h_{rib}) - 0.01\ \mu m] = 1.04\ \mu$m, located along a line from $x = (W_{pin}/2)$ to $x = [(w_{rib}/2) + w_{sep}]$ for one doped region and from $x = -(W_{pin}/2)$ to $x = -[(w_{rib}/2) + w_{sep}]$ for the other one, and a standard deviation along the y axis of 0.05 μm. At $x > -[(w_{rib}/2) + w_{sep}]$ for one doped region and $x < [(w_{rib}/2)+w_{sep}]$ for the other one, the doping drops off laterally (along the x axis) with a standard deviation of 0.035 μm. The length of the highly doped regions is equal to that of the cavity (L_{cav}). Metal electrodes contact both the p^+ (anode) and n^+ (cathode) regions with the same width and length as those. A planar silicon dioxide layer covering the whole structure has been assumed.

III. DEVICE MODEL

The electrooptic device was electrically and optically modeled. An electrical model was used to study key parameters of the p-i-n/cavity that determine the device performance, such as

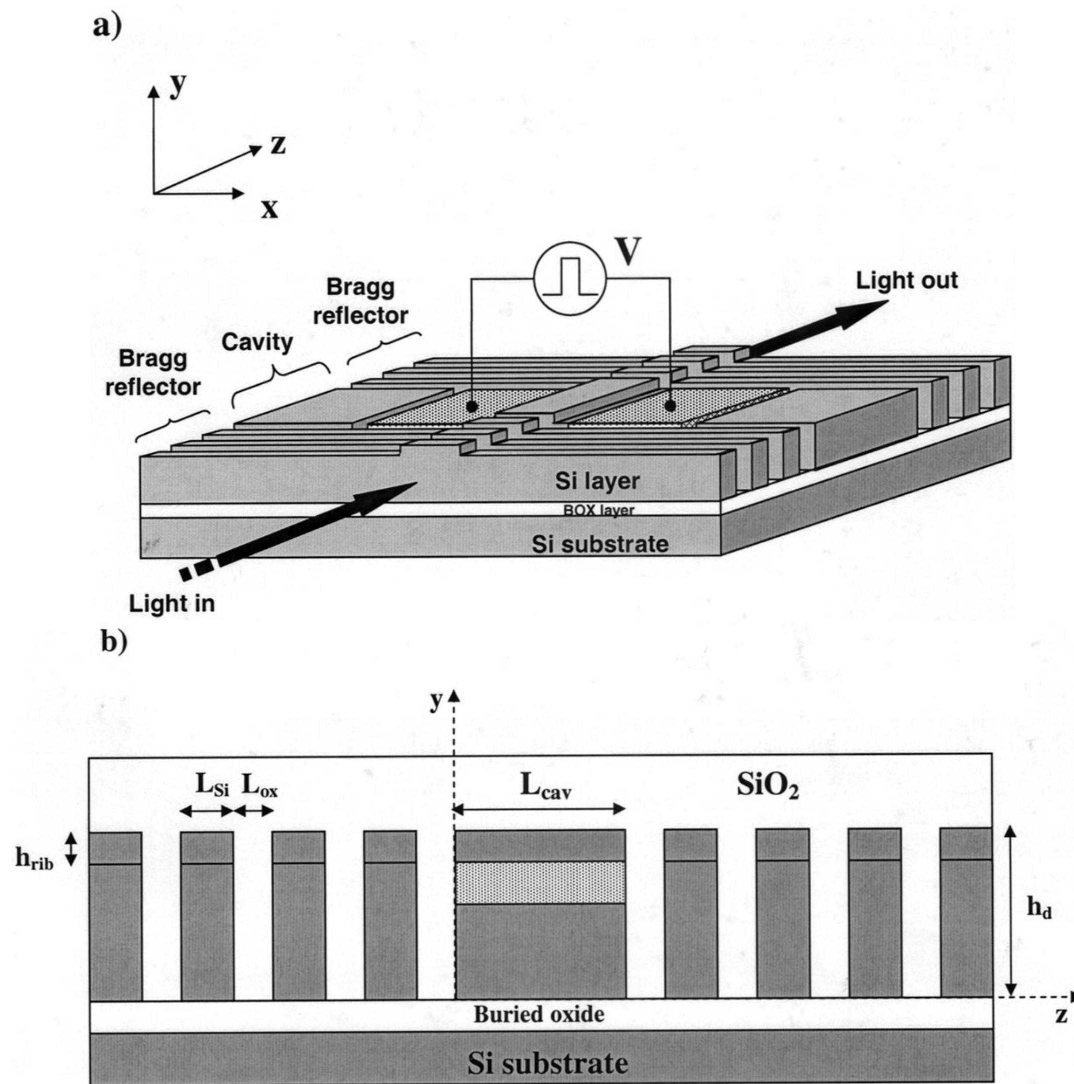

Fig. 1. (a) Silicon electrooptic modulator based on a p-i-n electrical structure in a Fabry–Pérot microcavity with high-reflectivity Bragg reflectors integrated in a single-mode SOI ridge waveguide. The output light is electrically controlled by a voltage generator (V). (b) Longitudinal cross section of the device.

free-carrier concentration and distribution in the cavity, injection current density, electrical power, and internal temperature under dc and transient conditions. An optical model was employed to design and analyze the Bragg reflectors and the cavity length in terms of transmission, modulation depth, and optical losses of the structure.

A. Electrical Model

A commercially available two-dimensional (2-D) and three-dimensional (3-D) simulation package, ATLAS from SILVACO [26], was employed to achieve the electrical calculations. The suitability of this device modeling software to analyze EOMs in SOI waveguides has been demonstrated by other authors [24], [27]. This program simulates internal physics and device characteristics of semiconductor devices by solving Poisson's equation and the charge continuity equations for electrons and holes numerically. The software allows a complete statistical approach (Fermi–Dirac statistics) when, for example, heavily doped regions are considered. Carrier recombination models include Shockley–Read–Hall (SRH) recombination, Auger recombination, and surface recombination. A concentration– and temperature-dependent model has been used to model the carrier mobility. The simulation package also includes thermal modeling, which accounts for Joule heating, heating and cooling due to carrier generation and recombination, and the Peltier and Thomson effects. The heat flow equation is solved for specific combinations of heat-sink structures, thermal impedances, and ambient temperatures.

In our simulations, a carrier concentration-dependent SRH recombination model has been employed, with an estimated carrier lifetime in the Si device layer (intrinsic region) of electrons and holes of $\tau_n = 700$ ns and $\tau_p = 300$ ns, respectively, for an n-type doping concentration of 10^{15} cm^{-3} [18].

Ohmic contacts without additional contact resistance or capacitance have been assumed. In addition, the electrical contacts (electrodes) were considered to act as thermal contacts (heat sinks) at a fixed temperature of 300 K.

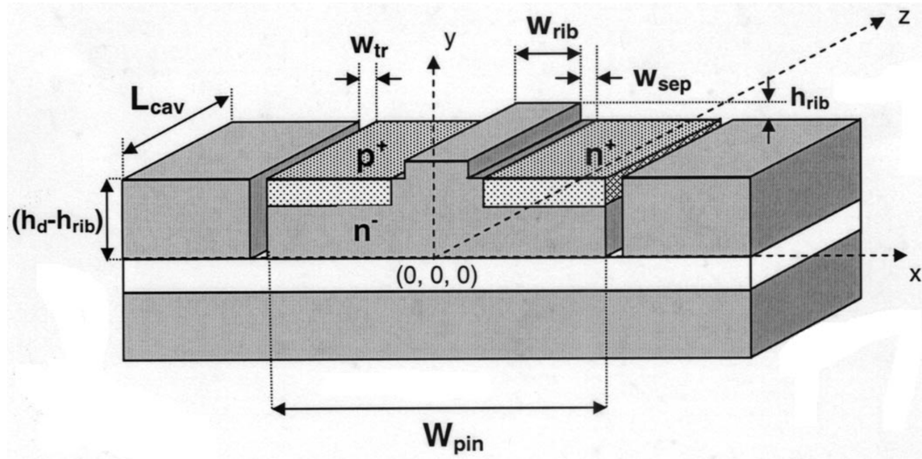

Fig. 2. Schematic of the microcavity. A lateral p-i-n diode is formed by defining two highly doped n and p regions at each side of the ridge, respectively. Two lateral trenches avoid carrier diffusion away from the cavity region.

B. Optical Model

We used the finite-difference time-domain (FDTD) method [28] and transfer matrix method (TMM) [29] for the optical analysis of the DBRs and F-P cavity. From the values of the electron and hole concentrations at any point of the p-i-n/cavity region, the induced real refractive index and optical absorption coefficient variations (Δn and $\Delta\alpha$, respectively) at a wavelength of 1.55 μm produced by free-carrier dispersion (highly doped regions and carrier injection in the cavity) are calculated by using [30]

$$\Delta n = \Delta n_e + \Delta n_h = -\left[8.8\times 10^{-22}\cdot \Delta N + 8.5\times 10^{-18}\cdot (\Delta P)^{0.8}\right] \quad (1)$$

$$\Delta\alpha = \Delta\alpha_e + \Delta\alpha_h = 8.5\times 10^{-18}\cdot \Delta N + 6.0\times 10^{-18}\cdot \Delta P \quad (2)$$

where

Δn_e	refractive-index change due to electron concentration change;
Δn_h	refractive-index change due to hole concentration change;
ΔN	electron concentration change in cm^{-3};
ΔP	hole concentration change in cm^{-3};
$\Delta\alpha_e (\mathrm{in\ cm}^{-1})$	absorption coefficient variations due to ΔN;
$\Delta\alpha_h (\mathrm{in\ cm}^{-1})$	absorption coefficient variation due to ΔP.

Diffraction losses and material optical absorption are calculated with the FDTD method. The fundamental mode of the waveguide is launched at the input and the reflected (R), and transmitted (T) powers are recorded by virtual detectors. Losses (A) are obtained by using the relation $R + T + A = 1$. Scattering losses, due to surface roughness, are neglected. We used a one-dimensional (1-D) model (along the propagation direction) based on the TMM to calculate the transmission and reflection spectra of the structure. The effect of the transverse and lateral geometry of the structure, the diffraction, and the absorption are considered in our 1-D model by using an equivalent complex effective refractive index obtained from the 3-D FDTD calculations of the entire structure for a short cavity length ($\lambda_p/2n_{\mathrm{Si}}$, where $\lambda_p = 1.55$ μm and n_{Si} is the effective refractive index of the Si region). The purpose of using this technique is to simplify the calculations by employing a flexible model that allows predicting the optical performance of the device for different design parameters in a shorter time. Calculations obtained by using this FDTD-assisted TMM technique were in good agreement with those obtained by employing exclusively the FDTD method, which supports the suitability of our model.

IV. Results and Discussion

A. Electrical Analysis

1) DC Characteristics: We found that both electron (N) and hole (P) concentrations in the cavity region are nearly equal for forward-bias voltages between 0.8 and 1.1 V, assuming a surface recombination velocity of 10^2 cm/s at the interface between the Si cavity and the surrounding SiO_2. This surface recombination velocity may correspond to Si surfaces passivated with thermally grown SiO_2 [31]. The p-i-n diode operates under high injection condition within the considered forward-bias voltage range. As expected from previous works on larger structures [17], [27], the injected carrier distribution is highly uniform throughout the central region of the cavity. This result simplifies the optical calculations, since the spatial distribution of the refractive index and absorption coefficient in the cavity when carriers are injected in the guiding region can be considered uniform. A carrier concentration of $N = P = 3\times 10^{17}$ cm^{-3} is predicted for a forward bias of 0.87 V, which induces a real refractive-index change of $\Delta n = -10^{-3}$ [see (1)] and an absorption coefficient variation of $\Delta\alpha = 4.35$ cm^{-1} [see (2)].

Our simulations show that some of the injected free carriers into the low-doped n-type Si layer spread laterally away from the central guiding region as the distance between the lateral trenches (W_{pin}) is increased, in agreement with previous works [24]. This leads to a leakage current component that increases the necessary dc power in order to obtain the targeted carrier concentration (refractive-index change) in the central guiding region. In particular, the dc power consumption for

TABLE II
TOTAL CURRENT DENSITY (J), PERCENTAGE OF THE CURRENT COMPONENT DUE TO SURFACE RECOMBINATION (J_s) TO THE TOTAL CURRENT (J), DC ELECTRICAL POWER (P_{dc}), AND FREE-CARRIER CONCENTRATION (N, P) IN THE CENTRAL REGION OF THE CAVITY FOR THREE SURFACE RECOMBINATION VELOCITIES AT THE Si/SiO_2 INTERFACES: (a) $S_p = S_n = 0$; (b) $S_p = S_n = 10^2$ cm/s; AND (c) $S_p = S_n = 10^5$ cm/s. A FORWARD-BIAS VOLTAGE OF 0.87 V AND A CAVITY LENGTH OF 1 μm ARE CONSIDERED

S_p, S_n (cm/s)	J (A/cm^2)	J_s/J (%)	P_{dc}(μW)	N, P (cm^{-3})
0	83.33	0	1.14	3x10^{17}
10^2	115.86	28.1	1.51	3x10^{17}
10^5	5514.6	98.5	71.9	5x10^{16}

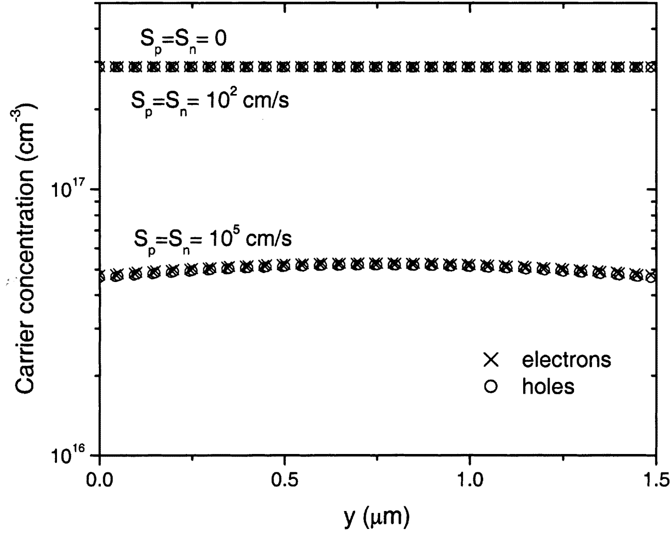

Fig. 3. Free-carrier distribution along the y axis at $x = 0$ μm and $z = L_{cav}/2$ for three different surface recombination velocities at the Si/SiO_2 cavity interface: (a) $S_p = S_n = 0$; (b) $S_p = S_n = 10^2$ cm/s; and (c) $S_p = S_n = 10^5$ cm/s. In all cases, a forward-bias voltage of 0.87 V is considered.

W_{pin} equal to 4.5, 8, and 12 μm was calculated to be 0.81, 1.51, and 2.27 μW per micrometer length, respectively, for a free-carrier concentration in the cavity of 3×10^{17} cm^{-3}. That is, the dc power increases 180% when W_{pin} is varied from 4.5 to 12 μm, indicating the need to confine carriers in the guiding region in order to reduce the drive dc power. Hereafter, we will assume a W_{pin} value of 8 μm as a compromise between low power consumption and good optical properties [see Section IV-B1)]. In the same way as occurs in the lateral direction (x axis), carriers may diffuse along the longitudinal direction (z axis) if no carrier confinement means are accounted. By using lateral and longitudinal trenches down to the BOX layer, electrical isolation of the cavity is achieved along all directions, leading to injection carrier confinement in the central guiding region, suppressing the leakage current due to carrier spreading.

Fig. 3 shows the electron and hole distribution along the y axis at $x = 0$ μm and $z = L_{cav}/2$ for a forward-bias voltage of 0.87 V and different surface recombination velocities (S_p and S_n, for holes and electrons, respectively). In case (a), no surface recombination ($S_p = S_n = 0$) is assumed; case (b) corresponds to thermally grown SiO_2 ($S_p = S_n = 10^2$ cm/s); and case (c) assumes no surface passivation ($S_p = S_n = 10^5$ cm/s). As expected, it is observed that for case (a), the carrier distribution is highly uniform. For case (b), the carrier distribution is not significantly affected with respect to case (a). On the other hand, for case (c), it is clear that the total carrier concentration has decreased with respect to the previous cases and does not present a uniform spatial distribution. Case (c) could correspond to a Si/SiO_2 interface in which SiO_2 has been placed by means other than thermal growth, such as, for example, chemical vapor deposition (CVD) or spin-on-glass (SOG) techniques.

Table II shows the drive current density (J), percentage of the current component due to surface recombination (J_s) to the total current (J), dc power (P_{dc}), and free-carrier concentration (N, P) in the central region of the cavity for the aforementioned surface recombination velocities. The current density is defined as the total injection current divided by the longitudinal cross-section area of the cavity at the middle ($x = 0$). In all the cases, a forward voltage of 0.87 V and a cavity length of 1 μm are assumed.

As expected, it is seen that the injection current and electrical power increase as the surface recombination velocity is increased. For case (b), the injection current component due to surface recombination (leakage current) represents 28.1% of the total current, whereas this leakage component reaches a significant 98.5% of the total injected current for case (c). The dissipated power for case (b) increases by 32.4%, as compared with case (a), as a consequence of leakage current via surface recombination; nevertheless, the total drive power is kept to a low value. These results indicate the importance of electrical passivation of the surfaces of the p-i-n/cavity region in order to reduce the component of the total current due to surface recombination and, therefore, the dc power consumption. In addition, surface passivation by thermal SiO_2 is also advantageous from the optical point of view, since it reduces the scattering losses from the surface [32]. Hereafter, a surface recombination velocity of $S_p = S_n = 10^2$ cm/s will be assumed. For this case, the calculated increase of the device temperature was less than 10^{-2} K.

It must be noted that the effect of the contact resistance of the electrodes on the total power is not significant for a forward injection current of 1.74 $\mu A/\mu m$ ($V = 0.87$ V) if proper contact metallization is achieved. For example, if Co/Si contacts are assumed on both electrodes, the corresponding contact resistance values, after a rapid thermal annealing (RTA) process, on the highly doped n^+ and p^+ regions should be around 1.6×10^{-7} and 8.9×10^{-7} Ωcm^2, respectively [33]. This means a total series resistance due to the contacts of 38.2 Ω μm, which leads to a negligible increase of 1.1×10^{-10} W/μm in dc power consumption.

B. Transient Characteristics

We assumed an excitation voltage pulse with $V_{OFF} = 0$ V (OFF state) and $V_{ON} = 0.87$ V (ON state) for the transient analysis. The duration of both OFF and ON states is 300 ns,

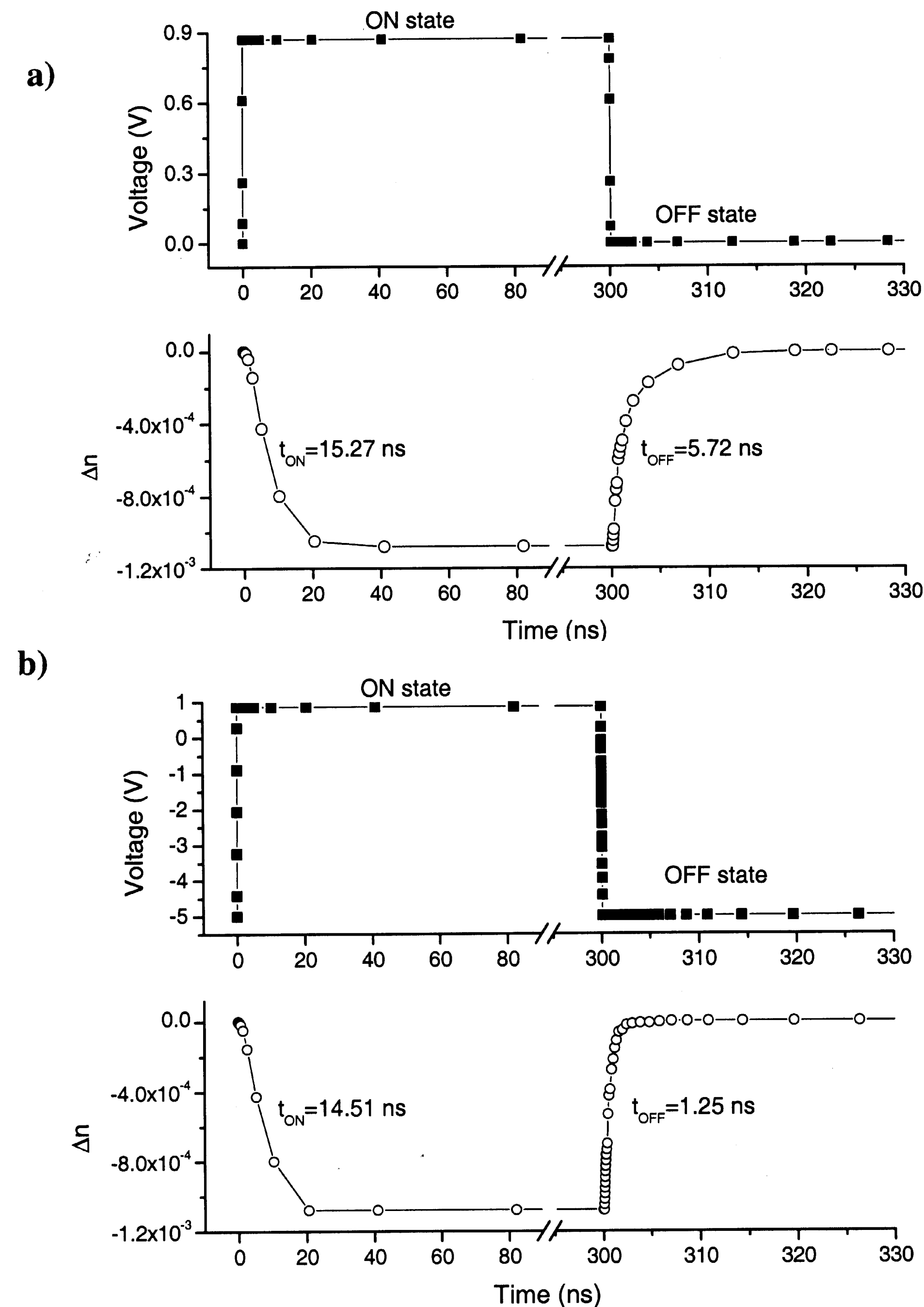

Fig. 4. (a) Transient behavior of the refractive-index change in the cavity (Δn) for a voltage pulse with $\mathrm{V_{ON}} = 0.87$ V and $\mathrm{V_{OFF}} = 0$ V. (b) Transient variation of Δn for $\mathrm{V_{ON}} = 0.87$ V and $\mathrm{V_{OFF}} = -5$ V. In both cases, the voltage pulse is 300 ns long for both ON and OFF states with ramp and fall times of 0.1 ns.

whereas both the rise time and fall time for the voltage bias step are 0.1 ns. Fig. 4(a) shows the excitation voltage pulse and the calculated refractive-index modulation (Δn) in the cavity due to free-carrier dispersion effect versus time. For the refractive-index modulation, we define the turn-on time (t_{ON}) as the time required for the refractive-index change (Δn) to change from 10% to 90% of its maximum absolute value $(|\Delta n|)$. Likewise, the turn-off time (t_{OFF}) is defined as the time needed for the refractive-index change to vary from 90% to 10% of its maximum absolute value. It is seen that the turn-on time is longer than the turn-off time. The decrease of refractive index occurs because of carrier injection (forward bias) by diffusion from the highly doped regions into the intrinsic (low-doped) material. This is because the characteristic length for diffusive transport in the intrinsic region $l = (D_a \tau_{\mathrm{eff}})^{1/2} = 5.2\ \mu\mathrm{m}$ [$D_a = 18\ \mathrm{cm}^2/\mathrm{s}$ is the ambipolar diffusion coefficient [9], and τ_{eff} $(= t_{\mathrm{ON}} = 15.27$ ns) is the effective carrier lifetime in the intrinsic region] is comparable to the lateral dimension of our device. On the other hand, the increase of refractive index results from depletion of carriers in the central guiding region. Carrier removal is achieved by both carrier recombination and the increased electric field across the intrinsic region. A higher reverse $\mathrm{V_{OFF}}$ would result in a shorter turn-off time, since the depletion electric field is increased. This is seen in Fig. 4(b) for

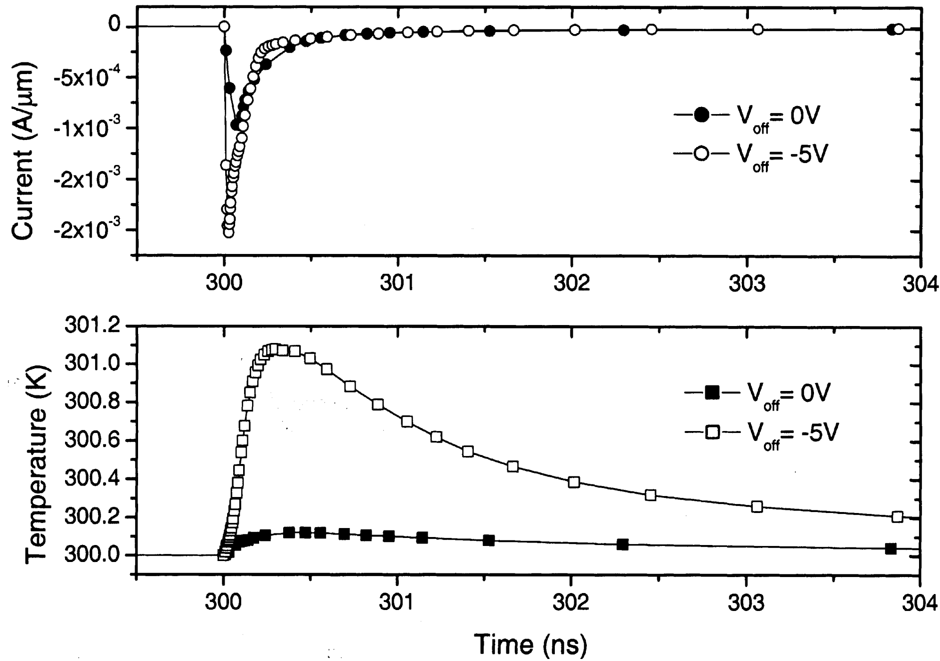

Fig. 5. Current and maximum device temperature transient response when the device is switched off from $\mathrm{V_{ON}} = 0.87$ V to $\mathrm{V_{OFF}} = 0$ V (filled circles and squares, respectively) and from $\mathrm{V_{ON}} = 0.87$ V to $\mathrm{V_{OFF}} = -5$ V (open circles and squares, respectively). The temperature of the thermal contacts (electrodes) is 300 K.

$\mathrm{V_{OFF}} = -5$ V. The simulations reveal that both voltage rise and fall processes lead to the appearance of current peaks for a short time interval. In particular, a remarkable reverse current peak occurs during the transition from $\mathrm{V_{ON}}$ to $\mathrm{V_{OFF}}$. Fig. 5 shows the transient current and maximum device temperature during the stepping down of the applied voltage from $\mathrm{V_{ON}} =$ 0.87 V to $\mathrm{V_{OFF}} = 0$ V and -5 V. In both cases, it is observed that the transient reverse current peak (2×10^{-3} and 1×10^{-3} A/μm for $\mathrm{V_{OFF}} = -5$ V and $\mathrm{V_{OFF}} = 0$ V, respectively) is around three orders of magnitude higher than the corresponding steady-state current (1.74 μA/μm), and the maximum current for $\mathrm{V_{OFF}} = -5$ V is twice higher than that reached for $\mathrm{V_{OFF}} = 0$ V. The higher the reverse $\mathrm{V_{OFF}}$, the shorter becomes the rise time and the larger the transient current peak. This leads to an appreciable increase of the device temperature, around 1 K for $\mathrm{V_{OFF}} = -5$ V. For $\lambda = 1.55$ μm, the thermal change of refractive index of silicon is $\partial n/\partial \mathrm{T} = +1.86 \times 10^{-4}$ $\mathrm{K^{-1}}$ [5]. That is, a maximum temperature increase of 1 K corresponds to an increase of the refractive index of $+1.86 \times 10^{-4}$, which is one order of magnitude smaller than that induced by the free-carrier dispersion ($\Delta n = -10^{-3}$). Therefore, the thermooptic effect for both $\mathrm{V_{OFF}} = 0$ V and $\mathrm{V_{OFF}} = -5$ V is predicted to be not significant.

Another factor that could limit the switching time of the device is the photon lifetime in the F-P cavity. The photon lifetime (τ_{ph}) corresponds to the time for the stored energy in the cavity to vanish after the external supply is shut off. However, the photon lifetime values for the considered device configurations [see Subsection IV-B2)] are calculated to be on the order of tens to hundreds of picoseconds, that is, much shorter than the switching times obtained in the electrical transient analysis. Therefore carrier diffusion, for the turn-on time, and carrier depletion, for the turn-off time, should be pointed out as the switching speed limiting factors in the device under study.

It must be noted that a larger value of W_{pin} would increase the switching time (t_s) since the refractive index must be changed (carrier injection and depletion) in a larger volume. For example, the calculated t_s for $W_{\mathrm{pin}} = 12$ μm, $\mathrm{V_{ON}} = 0.87$ V and $\mathrm{V_{OFF}} = -5$ V is predicted to be 18.56 ns, that is, 17.7% larger than that calculated for $W_{\mathrm{pin}} = 8$ μm.

C. Optical Analysis

1) Modal Characteristics: Our simulations show single-mode operation in the SOI rib waveguide for both transverse electric (TE) and transverse magnetic (TM) polarization modes, for $h_{\mathrm{rib}} = 0.45$ μm, $w_{\mathrm{rib}} = 1.5$ μm, and $h_{\mathrm{d}} = 1.5$ μm. The distance between the lateral trenches $W_{\mathrm{pin}} = 8$ μm was chosen in order to minimize the optical mode mismatch between the DBR and the cavity region, as well as the power consumption and switching time. Fig. 6 shows the intensity profile of the propagating fundamental TE mode ($\mathrm{TE_{00}}$) for $W_{\mathrm{pin}} = 8$ μm. The overlap integral between the $\mathrm{TE_{00}}$ mode in the cavity region and $\mathrm{TE_{00}}$ mode in the DBR region was calculated to be 99.99%. Lower W_{pin} values may lead to unstable single-mode operation. The free-carrier absorption losses of the propagating mode due to the highly doped $\mathrm{p^+}$ and $\mathrm{n^+}$ regions were found to be negligible because of the small overlap between these regions and the optical mode.

2) Transmission Characteristics: The lengths of the Si and $\mathrm{SiO_2}$ regions of the DBRs were chosen according to the condition $n_{\mathrm{Si}}L_{\mathrm{Si}} + n_{\mathrm{ox}}L_{\mathrm{ox}} = \lambda_{\mathrm{p}}/2$, where n_{Si} and n_{ox} are the effective refractive indexes of the Si and $\mathrm{SiO_2}$ re-

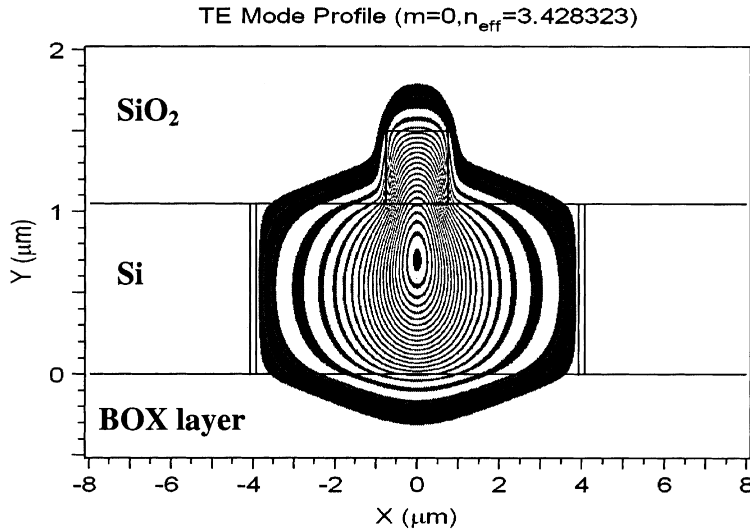

Fig. 6. TE_{00} mode distribution in the cavity for $W_{\mathrm{pin}} = 8$ μm, $h_{\mathrm{rib}} = 0.45$ μm, $w_{\mathrm{rib}} = 1.5$ μm, and $h_{\mathrm{d}} = 1.5$ μm.

gions, respectively, and $\lambda_{\mathrm{p}} = 1.55$ μm. In particular, we chose $L_{\mathrm{Si}} = 160$ nm and $L_{\mathrm{ox}} = 150$ nm, which lead to an optical path $n_{\mathrm{ox}}L_{\mathrm{ox}}$ smaller than $n_{\mathrm{Si}}L_{\mathrm{Si}}$ in order to minimize diffraction losses. The calculated reflectivity spectrum for the TE_{00} mode of a 6 Si/SiO_2-period DBR indicated a stopband of ~800 nm and a maximum reflectivity of 98.7% (transmittivity = 0.57% and diffraction losses = 0.73%).

The modulation depth (M) is defined as

$$M = 1 - \frac{T_{\mathrm{MIN}}}{T_{\mathrm{MAX}}} = \frac{P_{\mathrm{OFF}} - P_{\mathrm{ON}}}{P_{\mathrm{OFF}}} \tag{3}$$

where $T_{\mathrm{MAX(MIN)}}$ is the maximum(minimum) transmittivity, i.e., the ratio between the output in the OFF(ON) state and the input power P_{OFF} is the output optical power from the device when there is no free-carrier injection (OFF condition), and P_{ON} is the output optical power from the modulator when plasma injection occurs into the cavity (ON condition). Hereafter, the maximum transmittivity will be called just transmitivitty (T). The output optical power is calculated at $\lambda_{\mathrm{p}} = 1.55$ μm (probe wavelength), which corresponds to a cavity resonance wavelength in the OFF condition. Table III shows the full-width at half-maximum (FWHM) of the spectral intensity ($\Delta\lambda$) of the resonance peak at 1.55 μm, modulation depth (M), transmittivity (T), and dc dissipated power (P_{dc}) for different cavity lengths and number of DBR periods. A refractive-index change in the cavity of $\Delta n = -10^{-3}$ is assumed. It is seen that 1) the modulation depth increases and 2) the transmittivity decreases as the number of periods is increased for a given cavity length. The first is due to the increase of the resonance peak sharpness (a decrease of $\Delta\lambda$) as a consequence of the increase of the DBR's reflectivity. The second is originated by the increase of the diffraction losses. The relation modulation depth—transmittivity is illustrated in Fig. 7, which shows the transmission characteristics of the device in the ON and OFF state for an $80(\lambda_{\mathrm{p}}/2n_{\mathrm{Si}})$-long cavity with three-period and four-period DBRs. Intensity attenuation due to the injected carriers in the ON state ($\alpha = 4.35$ cm^{-1}) is observed. Although the use of a specific configuration may depend on the specific application, a good tradeoff between modulation depth (80%) and transmittivity (86%) is obtained for a ~ 18 − μm-long cavity with three-period DBRs, which represents a total device length of ~ 20 μm. It must be noted the low values of the electrical power shown in Table III as well as the small refractive-index change in the cavity (0.1%) required to achieve high modulation depths.

TABLE III
TRANSMISSION CHARACTERISTICS OF THE Si ELECTROOPTIC MODULATOR FOR A REFRACTIVE-INDEX CHANGE IN THE CAVITY $\Delta n = -10^{-3}$, TE_{00} OPTICAL MODE, $L_{\mathrm{Si}} = 160$ nm, $L_{\mathrm{ox}} = 150$ nm, AND PROBE WAVELENGTH $\lambda_{\mathrm{p}} = 1.55$ μm: FWHM OF THE RESONANCE PEAK ($\Delta\lambda$), MODULATION DEPTH (M), TRANSMITTIVITY (T), AND dc DISSIPATED POWER (P_{dc}) FOR VARIOUS CAVITY LENGTHS AND NUMBER OF PERIODS OF THE DBRs

L_{cav} (μm)	periods	Δλ (nm)	M (%)	T (%)	P_{dc} (μW)
5.684 ($25\lambda_p/2n_{Si}$)	3	1.275	27.6	86.3	7.8
	4	0.396	82.3	59.3	
	5	0.170	93.8	21.4	
9.074 ($40\lambda_p/2n_{Si}$)	3	0.807	50.3	86.3	12.3
	4	0.251	89.8	59.3	
	5	0.108	98.4	21.4	
18.117 ($80\lambda_p/2n_{Si}$)	3	0.408	80.8	86.3	24.5
	4	0.127	97.7	59.3	
	5	0.055	99.6	21.4	
22.638 ($100\lambda_p/2n_{Si}$)	3	0.327	86.8	86.3	30.6
	4	0.102	98.5	59.3	
	5	0.044	99.7	21.4	

The feasibility of producing high-aspect-ratio trenches on SOI with high verticality has been demonstrated by other authors [34], [35]. Nevertheless, deviations from the considered dimensions of the optical structure (length of the DBRs and cavity) due to fabrication tolerances may affect the predicted device performance. We estimated the effect of fabrication errors on the spectral transmittance by calculating the transmittivity spectra for different length deviations of the structure using the effective-index method together with the TMM, and calculating their average. Fig. 8 shows the calculated spectral transmittivity for the case considered in Fig. 7 (three-period DBR) for a maximum length deviation of 20 nm (that is, $L_{\mathrm{Si}} = 160 \pm 10$ nm, $L_{\mathrm{ox}} = 150 \pm 10$ nm, and $L_{\mathrm{cav}} = 18.097 \pm 0.010$ μm), 10 nm, and 5 nm. The length deviation of the DBR and cavity was assumed to be the same

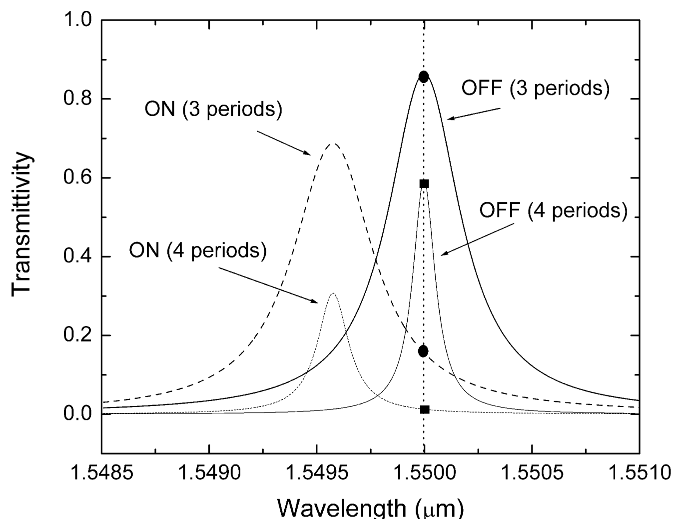

Fig. 7. Spectral transmittance for the TE_{00} optical mode of the simulated Si modulator in the OFF ($\Delta n = 0$) and ON ($\Delta n = -10^{-3}$) states for a three-period DBR device and a four-period DBR device. In both cases, the length of the cavity is $80(\lambda_{\mathrm{P}}/2n_{\mathrm{Si}}) = 18.1\ \mu$m. The circles and squares illustrate the modulation depth at $\lambda_{\mathrm{P}} = 1.55\ \mu$m for the three-period and four-period device, respectively.

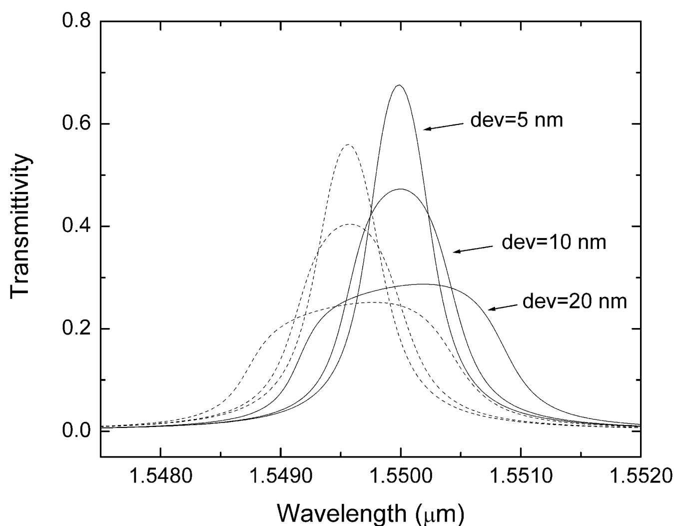

Fig. 8. Effect of length deviations of the DBR regions and cavity on the spectral transmittance with respect to the ideal case shown in Fig. 7 (three-period DBR). Maximum deviations (dev) of 20, 10, and 5 nm are considered. The OFF ($\Delta n = 0$) and ON ($\Delta n = -10^{-3}$) states are indicated by solid and dashed lines, respectively.

and the period of the DBR constant. It is seen that the resonance peak shape becomes degraded as the length deviation increases. This is mainly due to the variations of the cavity length, which shift the resonance wavelength for each length component, broadening the averaged resonance peak. As a consequence, the transmitivitty is considerably reduced as compared to the ideal case (see Fig. 7 for three-period DBR). It is also observed that high modulation depths can still be achieved ($\sim$72% at 1.5508-μm wavelength for a 20-nm-length deviation). Our simulations showed that if the considered length variations occur only in the DBR regions, the transmission spectrum is not significantly affected with respect to the ideal case.

V. Summary and Conclusion

We have analyzed the performance of a new planar silicon EOM based on an F-P microcavity by deep high-index-contrast $\mathrm{Si/SiO_2}$ Bragg reflectors and confinement of free-carrier plasma dispersion in an SOI rib waveguide. Free-carrier concentration change in the cavity region produced by an integrated lateral p-i-n diode induces a refractive-index change that modulates the output power at a 1.55-μm wavelength. Deep lateral trenches in the p-i-n/cavity region laterally confine the injected carriers into the cavity. Deep $\mathrm{Si/SiO_2}$ DBRs confine longitudinally 1) the free carriers and 2) the optical field into the cavity region. The device has been analyzed by using electrical and optical models.

Our analysis shows that a distance of $W_{\mathrm{pin}} = 8\ \mu$m between the cavity lateral trenches permits minimization of a) the dc electrical power and switching time of the device and b) the mode mismatch between the cavity and the DBRs. Electrical passivation of the cavity surfaces with thermal $\mathrm{SiO_2}$ ($S_p = S_n = 10^2$ cm/s) is predicted to reduce the leakage current due to surface recombination by 70% as compared with a nonpassivated surface cavity ($S_p = S_n = 10^5$ cm/s), without significantly affecting the injection carrier concentration as compared with the case of no surface recombination ($S_p = S_n = 0$ cm/s). Diffraction is found to be the main cause of optical power losses in our device for $\Delta n = -10^{-3}$ in the cavity. Calculations show that a tradeoff between modulation depth and transmittivity of the device must be considered.

A 20-μm-long device with $S_p = S_n = 10^2$ cm/s, $W_{\mathrm{pin}} = 8\ \mu$m, and electrical contacts acting as heat sinks is predicted to exhibit $\sim$80% of modulation depth with a transmittivity of $\sim$86% at 1.55-μm operation wavelength by using $\sim 25\ \mu$W of electrical power and a drive current density of 116 A/cm^2 under dc operation, leading to an increase of the device temperature $< 10^{-2}$K. The switching speed of this device is calculated to be $\sim$16 ns for $\mathrm{V_{ON}} = 0.87$ V and $\mathrm{V_{OFF}} = -5$ V, with no significant thermooptic effect. To our knowledge, the estimated dc power consumption for this device is at least one order of magnitude smaller than the smallest reported (theoretical) value [20]. These characteristics reveal the benefits of confining both the optical field and the injection carriers in the cavity region in order to improve the EOM performance in terms of power consumption, current density, device length, and modulation depth. Si CMOS process compatibility makes this device very promising for low-cost and low-power silicon-based integrated photonic systems on a chip (PSOC) for low-frequency applications, such as LANs, fiber-to-home return links, interconnects, and sensor systems for chemical and biochemical applications.

Acknowledgment

The authors thank Dr. R. Panepucci and B. Schmidt for useful discussions.

References

[1] R. A. Soref, "Silicon-based optoelectronics," *Proc. IEEE*, vol. 81, pp. 1687–1706, Dec. 1993.
[2] U. Fischer, T. Zinke, J.-R. Kropp, F. Arndt, and K. Petermann, "0.1 dB/cm waveguide losses in single-mode SOI rib waveguides," *IEEE Photon. Technol. Lett.*, vol. 29, pp. 647–648, May 1996.

[3] P. Trinh, S. Yegnanaray, and B. Jalali, "5 × 9 integrated optical start coupler in silicon-on-insulator," *IEEE Photon. Technol. Lett.*, vol. 8, pp. 794–796, 1996.
[4] T. W. Ang, G. T. Reed, A. Vonsovici, A. G. Evans, P. R. Routley, and M. R. Josey, "Effects of grating heights on highly efficient unibond SOI waveguide grating couplers," *IEEE Photon. Technol. Lett.*, vol. 12, pp. 59–61, Jan. 2000.
[5] G. Cocorullo and I. Rendina, "Thermo-optical modulator at 1.5 μm in silicon etalon," *Electron. Lett.*, vol. 28, no. 1, p. 83, 1992.
[6] C. Cocorullo, M. Iodice, I. Rendina, and P. M. Sarro, "Silicon thermo-optical micro-modulator with 700 kHz −3 dB bandwidth," *IEEE Photon. Technol. Lett.*, vol. 7, pp. 363–365, Apr. 1995.
[7] J. P. Lorenzo and R. A. Soref, "1.3 μm electro-optic silicon switch," *Appl. Phys. Lett.*, vol. 51, no. 1, p. 6, 1987.
[8] B. R. Hemenway, O. Solgaard, and D. M. Bloom, "All-silicon integrated optical modulator for 1.3 μm fiber-optic interconnects," *Appl. Phys. Lett.*, vol. 55, no. 4, p. 349, 1989.
[9] G. V. Treyz, P. G. May, and J.-M. Halbout, "Silicon optical modulators at 1.3 μm based on free-carrier absorption," *IEEE Electron Device Lett.*, vol. 12, p. 276, June 1991.
[10] ——, "Silicon Mach–Zehnder waveguide interferometers based on the plasma dispersion effect," *Appl. Phys. Lett.*, vol. 59, no. 7, p. 771, 1991.
[11] X. Xiao, J. C. Sturm, K. K. Goel, and P. V. Schwartz, "Fabry–Pérot optical intensity modulator at 1.3 μm in silicon," *IEEE Photon. Technol. Lett.*, vol. 3, p. 230, Mar. 1991.
[12] Y. L. Liu, E. K. Liu, S. L. Zhang, G. Z. Li, and J. S. Luo, "Silicon 1 × 2 digital optical switch using plasma dispersion," *Electron. Lett.*, vol. 30, no. 2, p. 130, 1994.
[13] Y. Liu, E. Liu, G. Li, S. Zhang, J. Luo, F. Zhou, M. Cheng, B. Li, and H. Ge, "Novel silicon waveguide switch based on total internal reflection," *Appl. Phys. Lett.*, vol. 64, no. 16, p. 2079, 1994.
[14] C. Z. Zhao, G. Z. Li, E. K. Liu, Y. Gao, and X. D. Liu, "Silicon on insulator Mach–Zehnder waveguide interferometers operating at 1.3 μm," *Appl. Phys. Lett.*, vol. 67, no. 17, p. 2448, 1995.
[15] M. Y. Liu and S. Chou, "High-modulation-depth and short-cavity-length silicon Fabry–Pérot modulator with two grating Bragg reflectors," *Appl. Phys. Lett.*, vol. 68, no. 2, p. 170, 1995.
[16] C. Z. Zhao, E. K. Liu, G. Z. Li, Y. Gao, and C. S. Guo, "Zero-gap directional coupler switch integrated into a silicon-on-insulator for 1.3-μm operation," *Opt. Lett.*, vol. 21, no. 20, p. 1664, 1996.
[17] A. Cutolo, M. Iodice, A. Irace, P. Spirito, and L. Zeni, "An electrically controlled Bragg reflector integrated in a rib silicon on insulator waveguide," *Appl. Phys. Lett.*, vol. 71, no. 2, p. 199, 1997.
[18] A. Cutolo, M. Iodice, P. Spirito, and L. Zeni, "Silicon electro-optic modulator based on a three terminal device integrated in a low-loss single-mode SOI waveguide," *J. Lightwave Technol.*, vol. 15, p. 505, Mar. 1997.
[19] C. Z. Zhao, A. H. Chen, E. K. Liu, and G. Z. Li, "Silicon-on-insulator asymmetric optical switch based on total internal reflection," *IEEE Photon. Technol. Lett.*, vol. 9, p. 1113, Aug. 1997.
[20] G. Coppola, A. Irace, M. Iodice, and A. Cutolo, "Simulation and analysis of a high-efficiency silicon optoelectronic modulator based on a Bragg mirror," *Opt. Eng.*, vol. 40, no. 6, pp. 1076–1081, 2001.
[21] R. A. Soref and B. R. Bennett, "Electrooptical effects in silicon," *IEEE J. Quantum Electron.*, vol. 23, p. 123, Jan. 1987.
[22] S. R. Giguere, L. Friedman, R. A. Soref, and J. P. Lorenzo, "Simulation studies of silicon electro-optic waveguides devices," *J. Appl. Phys.*, vol. 68, no. 10, p. 4964, 1990.
[23] G. Breglio, A. Cutolo, A. Irace, P. Spirito, L. Zeni, M. Iodice, and P. M. Sarro, "Two silicon optical modulators realizable with a fully compatible bipolar process," *IEEE J. Select. Topics Quantum Electron.*, vol. 4, p. 1003, Nov./Dec. 1998.
[24] P. D. Hewitt and G. T. Reed, "Improved modulation performance of a silicon p-i-n device by trench isolation," *J. Lightwave Technol.*, vol. 19, p. 387, Mar. 2001.
[25] J. Schmidtchen, A. Splett, B. Schuppert, K. Petermann, and G. Burbach, "Low-loss singlemode optical waveguides with large cross section in silicon-on-insulator," *Electron. Lett.*, vol. 27, pp. 1486–1488, 1991.
[26] SILVACO Int., , Santa Clara, CA.
[27] P. D. Hewitt and G. T. Reed, "Improving the response of optical phase modulators in SOI by computer simulation," *J. Lightwave Technol.*, vol. 18, p. 443, Mar. 2000.
[28] [Online]. Available http://www.rsoftinc.com/fullwave.htm
[29] S. G. Lipson, H. Lipson, and D. S. Tannhauser, *Optical Physics*, 3rd ed. Cambridge, U.K.: Cambridge Univ. Press, 1995.
[30] R. A. Soref and B. R. Bennett, "Kramers–Kronig analysis of E-O switching in silicon," *SPIE Integr. Opt. Circuit Eng.*, vol. 704, 1986.
[31] D. R. Lim, "Device integration for silicon microphotonic platforms," Ph.D. dissertation, Mass. Inst. Technol., Cambridge, 2000.
[32] K. K. Lee, D. R. Lim, and L. C. Kimerling, "Fabrication of ultralow-loss Si/SiO_2 waveguides by roughness reduction," *Opt. Lett.*, vol. 26, no. 23, pp. 1888–1890, 2001.
[33] O. Nakatsuka, T. Ashizawa, H. Iwano, S. Zaima, and Y. Yasuda, "Contact resistivities and electrical characteristics of Co/Si contact by rapid thermal annealing," in *Proc. Advanced Metallization Conf. 1998 (AMC 1998)*, vol. 784, Warrendale, PA, 1999, pp. 605–610.
[34] M. Naydenkov and B. Jalali, "Fabrication of high aspect ratio photonic bandgap structures on silicon-on-insulator," *Proc. SPIE*, vol. 3936, pp. 33–39, 2000.
[35] M. Wasilik and A. P. Pisano, "Low frequency process for silicon on insulator deep reactive ion etching," *Proc. SPIE*, vol. 4592, pp. 462–472, 2001.

Carlos Angulo Barrios received the degree of Telecommunications Engineer from the Universidad Politécnica de Madrid (UPM), Madrid, Spain, in 1998, and the Ph.D. degree from the Royal Institute of Technology (KTH), Stockholm, Sweden, in 2002. His dissertation focused on the fabrication, performance, and analysis of GaAs-based buried-heterostructure lasers with Al-free semi-insulating materials regrowth.

In May 2002, he joined the Nanophotonics Group at the School of Electrical and Computer Engineering, Cornell University, Ithaca, NY, as a Postdoctoral Fellow. His work includes design, fabrication, and characterization of integrated photonic devices.

Vilson Rosa de Almeida was born in Brazil. He received the B.S. (*magna cum laude*) and M.S. degrees, both in electrical engineering, from Instituto Tecnologico de Aeronautica (ITA), Sao Jose dos Campos, Brazil, in 1997 and 1998, respectively. He is currently working toward the Ph.D. degree in electrical engineering with Cornell University, Ithaca, NY.

From 1998 to 2000, he conducted research on optical fiber sensors at Instituto de Estudos Avancados (IEAv-CTA), Sao Jose dos Campos, Brazil. His research interest areas are nanophotonic devices, optical fiber sensors, and photonic crystals.

Michal Lipson received the Ph.D. degree in semiconductor microcavities from The Technion—Israel Institute of Technology, Haifa, in 1999.

Subsequently, she was a Postdoctoral Associate in the Department of Material Science, Massachusetts Insitute of Technology (MIT), Cambridge. Her research at MIT was concerned with the physics and applications of Si-based photonic structures for on-chip applications. In July 2001, she joined the School of Electrical and Computer Engineering, Cornell University, Ithaca, NY, where she is an Assistant Professor studying nanophotonic structures.